JOURNAL OF PROPULSION AND POWER
Vol. 9, No. 6, Nov.–Dec. 1993

Constrictor Flow Analysis of a Medium Power Hydrogen Arcjet

B. Glocker* and M. Auweter-Kurtz†
Institut für Raumfahrtsysteme, Universität Stuttgart, 7000 Stuttgart 80, Germany

In a thermal arcjet the main heating of the propellant takes place in the constrictor. To gain more insight into arcjet operation and to obtain experimental data on the shape, size, and stability of the arc channel inside the constrictor, a modified arcjet thruster was built. Through a window in the nozzle throat the discharge channel in the constrictor was observed. With a fast CCD camera, images of the arc were taken, and using image processing methods a hydrogen arc was analyzed. The camera system was calibrated to measure absolute intensities. Thus, it was possible to determine the two-dimensional temperature profiles from electron continuum and from the line intensity ratio of the H_α and the H_β line. In the second section, an analytical method to calculate the flow conditions inside the constrictor is described. The first version of the model is developed for hydrogen as propellant. The calculation results are compared with measurements.

Nomenclature

A = area, m²
$\boldsymbol{B}$ = magnetic induction, Vs/m²
c = thermodiffusivity of cold gas, m²/s
c_h = total heat capacity, J/kgK
E = excitation energy, J
f = absorption oscillator strength
g = statistical weight
I = arc current, A
j = current density, A/m²
M = molecular mass, kg/mol
Ma = Mach number
$\dot{m}$ = mass flux, kg/s
n = grade of current density parabolic
n = particle density, l/m³
p = static pressure, N/m²
$\boldsymbol{q}$ = heat flux, W/m²
$\mathcal{R}$ = universal gas constant, J/molK
RL = radiation and reaction losses, W/m³
r = radius, m
T = temperature, K
v = velocity, m/s
z = coordinate in flow direction, m
δ_r = radial step in cold gas contour calculation, m
$\zeta, \bar{\zeta}$ = dimensionless quantities accounting for radiation losses
κ = adiabatic exponent
λ = heat conduction coefficient, W/mK
λ = wavelength, m
ν = frequency, l/s
ρ = mass density, kg/m³
σ = electric conductivity, A/Vm

Indices
a = arc core
c = cold gas layer
e = end of nozzle, electron
r = radial
t = end of constrictor
tr = transition region
$\hat{}$ = value at the centerline

Received Aug. 6, 1992; revision received March 21, 1993; accepted for publication April 23, 1993.

*Project Engineer. Member AIAA.
†Professor. Member AIAA.

Introduction

IN a thermal arcjet the electric arc discharge increases the enthalpy of the propellant flowing through a supersonic nozzle. The thruster consists of a coaxial electrode system which supports an electric discharge within an axial gaseous propellant stream. In the nozzle the thermal energy is converted into directed kinetic energy. With this device it is possible to achieve specific impulses which are higher by a factor of 2 compared to those of conventional chemical thrusters with the same propellant.

The main energy input into the propellant takes place in the constrictor. Therefore, it is essential to get more information about the dimension and temperature of the electrical discharge. Because of the small dimensions and the high temperature involved, only very few experiments have been conducted to determine the arc behavior inside the thruster.[1–4] In this work an experimental setup with a modified water-cooled thruster to investigate the behavior of the arc in the constrictor is described. Two-dimensional temperature profiles of the arc inside the constrictor are presented, using an image processing system with the help of small band interference filters. Hydrogen has been selected as propellant because the emission spectrum of this gas and the thermodynamic properties are well known, and with this propellant the highest specific impulses and best efficiencies can be achieved.[5]

In order to reduce the number of expensive experiments and to get an insight into the physics of a thermal arcjet, a calculation model is needed. The physical process in such devices is very complex and not fully understood today. In the early 60s a first attempt was made to model the constrictor conditions by dividing the flow in the constrictor into two regions with homogenic properties.[4] Fully three-dimensional numerical codes for the calculation of the flow through a hydrogen thruster have been started in recent years,[6,7] but at present no performance prediction can be made from these attempts.

In the second part of this work, a three-channel model, derived from the dual channel model presented in Ref. 8 is described, which is based on the knowledge gained from experimental investigations of the constrictor conditions. The emphasis in developing this computational method was put on modeling the physics of the convectively cooled arc in the constrictor in order to get a design instrument which allows numerical calculations at low computer costs.

Experiments

Thruster Modifications

The water-cooled laboratory thruster[9] is built as a stack of coaxial ring segments which define the contour of the injection

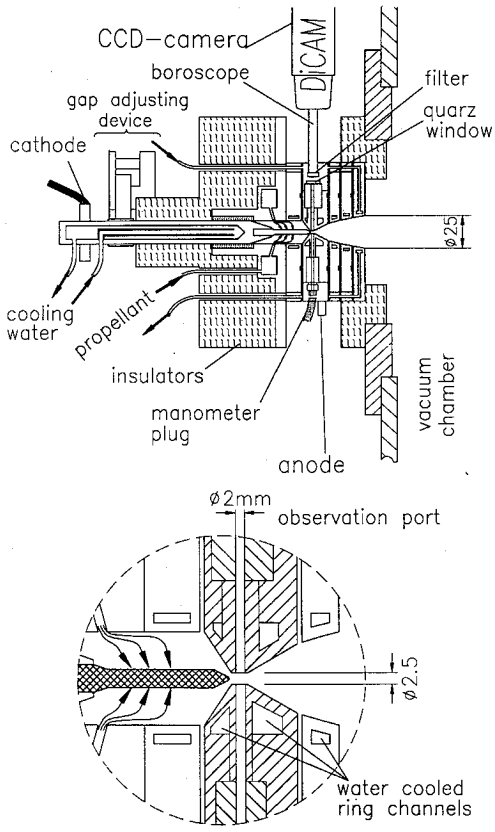

Fig. 1 Experimental schematic for the observation of the arc.

chamber, the nozzle throat, and the expansion section. All segments have separate water cooling loops to preserve the modularity of the engine. Electric arcing between adjusted segments is suppressed through the use of ceramic spacers which create a gap of 0.5 mm. Two radial holes on opposite sides of the constrictor segment allow a direct observation of the arc burning inside the constrictor. The holes have a diameter of 2 mm which may be compared to the dimensions of the constrictor (diameter: 2.5 mm, length: 5 mm). Therefore, almost the complete channel diameter is observable. The axial position of the viewing point is 2.6-mm downstream of the cathode tip. The bore hole is about 0.2-mm off center, allowing the observation of the constrictor wall.

In the regular mode of observation, there is only one viewpoint for optical access through a quartz glass window. A pressure gauge on the other access port measures the pressure inside the constrictor, another quantity of interest. Nevertheless, since it helps to suppress reflections inside the channel, this second hole is also required for the optical access. The walls of the radial holes were roughened to minimize reflection inside the channel. The overall configuration of the modified thruster is depicted in Fig. 1.

Optical Acquisition System

In order to observe the discharge in the constrictor channel, a video camera is used in connection with a magnifying borescope (Fig. 1). The spectral resolution in this experiment was achieved with several interference filters of approximately 10-nm bandwidth each. The camera consists of a regular CCD video module (768 × 512 pixels) coupled to a microchannel plate intensifier (MCP). The MCP has two functions: 1) it amplifies the received image and 2) it works as a very fast optical shutter with exposure times down to 20 ns. These two features make it possible to look at the bright discharge without alternating filters for intensity control and to acquire short exposures at frame rates up to 6 frames/s. A video digitizer is used to sample the images which are then available for online processing and storage on a computer. The borescope has a working distance of around 54 mm and a magnification of 50, thus creating a sufficiently large image for the MCP camera. The complete camera/borescope assembly is mounted on a linear traverse driven by a stepper motor. Using this mechanism, the camera can be retracted from the viewpoint for filter changes and positioned with a high degree of repeatability. The motor as well as the camera are remotely controlled to allow for gain, exposure, and focus adjustments while the engine is running.

The whole system camera, borescope, intensity filter, and quartz glass window was calibrated for absolute intensity measurements against a tungsten band lamp. The dependency of the intensity on the exposure time was determined and considered, and the nonlinearity of the system in intensity was analyzed by using different neutral density filters with measured transmissivity. This calibration was done separately for each intensity filter with the same setup as for the experiment. The bandwidth of the filters and their transmission characteristic, depending on the wavelength, were measured.

Experimental Procedures

The arcjet was ignited with the camera in a retracted position for safety reasons. Once the arcjet had reached its operating point, the camera was moved into position. First, images were taken without any optical filters, giving a broadband view of the arc. The shortest possible exposure time of 20 ns was used. For the temperature analysis, this procedure was repeated with the interference filters in front of the borescope. For this experiment the gain was set at the same level as for the calibration and the exposure time was selected to utilize the full resolution range of the camera (8 bit). Then a filter centered at 600 nm was used to measure the intensity of the electron continuum. It was ensured that at this wavelength the continuum radiation was not superimposed by spectral lines or wings of lines. The exposure time with this filter was 40 ms. Then measurements were done with a filter centered on the H_α, H_β, and H_γ line in the hydrogen spectrum. The exposure times were 0.2 ms for the H_α, 1 ms for the H_β, and 15 ms for the H_γ measurements. To determine temperatures from the intensity ratios of the lines, radial profiles from two different images has been compared. In order to eliminate the arc fluctuation and the noise superimposed on the profiles, a form signal averaging was applied, usually taking the 200 single exposures as the data ensemble. To compensate the arc fluctuations, averaging was done following a shift of the individual profiles to eliminate their relative centerline displacements. This helped to reduce the broadening of the arc intensity boundaries, an undesirable effect of averaging in general.

Thruster Operation Points

Table 1 shows the results of the general arcjet behavior for the investigated operation conditions. Three current settings were investigated for the low mass flow rate. The electrical input power varied from 6.77 to 8.62 kW. With the higher mass flow rate only two points were investigated at a power of 10.5 and 11.8 kW. The experimental procedure required that the thruster be shut off before filter changes. The reproducibility of all measured values was very good, the deviations were less than 1%.

Table 1 Investigated operation points of the thruster

$\dot{m}$, g/s	Current, A	Voltage, V	Arc chamber pressure, mbar	Constrictor pressure, mbar
0.1	50.2	134.9	968.8	740.0
0.1	60.3	128.7	986.0	766.9
0.1	70.6	122.1	1004.0	807.7
0.2	59.4	177.0	1585.6	1128.6
0.2	70.6	167.9	1622.0	1182.0

There are almost no differences in the current voltage characteristics to those of the standard TT1 thruster.[9] The pressure inside the constrictor is an important value to determine the thermodynamic properties for the spectroscopic analysis. As expected, it is smaller than the pressure in the upstream arc chamber section.

Arc Behavior

Using short exposure times (20 ns) of the image acquisition system, fluctuations of the position of the arc within the constrictor channel could be identified. Figure 2 shows a typical image which shows the geometry of the constrictor size and the cathode position. The line profile positions are given by the vertical line markers.

A first important result from the image is that the arc did not fill the constrictor completely. For hydrogen as propellant there was a rather large nonluminous gas layer surrounding the hot discharge core. Images taken with short exposure time revealed that the arc column fluctuates in position and size. By statistical methods the fluctuations were analyzed from 200 single profiles. The off center fluctuation was about 0.04 mm (standard deviation of the centerline position). Comparing the fluctuations of different thruster operation points, it was found that the magnitude of the centerline fluctuations increased with increasing mass flow rate and the arc was more stable with increasing current.[9] With the longer exposure times the arc fluctuations caused a smeared image.

A typical image from an experiment where the cathode was not properly centered is shown in Fig. 3. In this experiment the cathode was somewhat shifted upward on the left side of the image. This resulted in a shifted arc column which became centered more downstream by hydrodynamic forces. Also, the radial intensity profiles were not symmetric, but they re-

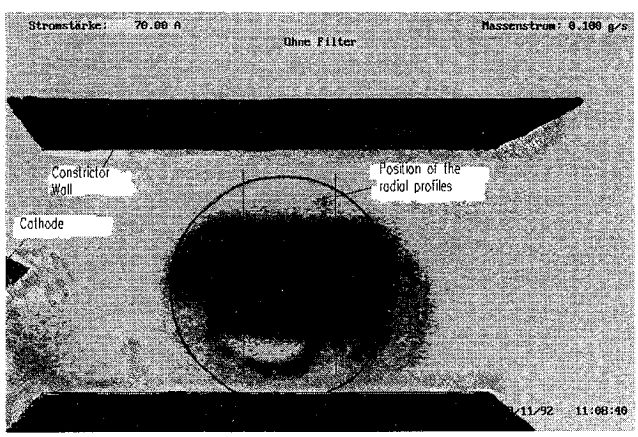

Fig. 2 Illustration of the arc in the constrictor and the geometrical dimensions. I = 70 A, m = 0.1 g/s, exposure time 20 ns.

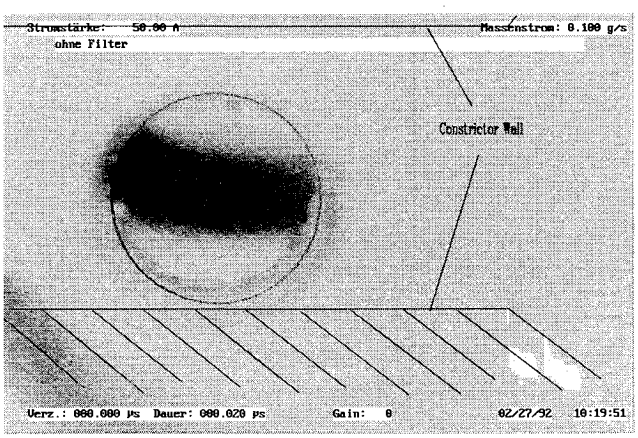

Fig. 3 Asymmetrical cathode I = 50 A, m = 0.1 g/s.

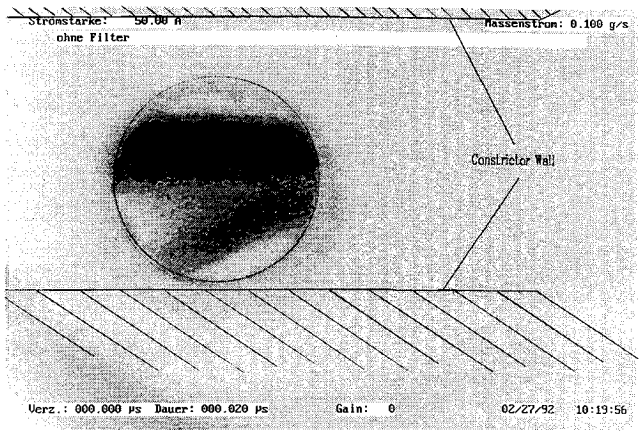

Fig. 4 Anomalous anode attachment in the constrictor I = 50 A, m = 0.1 g/s.

gained symmetry further downstream. With the eccentric cathode the arc fluctuated more than with a well centered one.

A few images showed an anode attachment of the arc within the constrictor. Since the bore hole was off center, this attachment could be observed. Figure 4 shows such an image. In a previous measurement[10] of the current distribution at the anode it was found that the arc attachment was mostly located in the supersonic part of the anode, and only minor current is conducted through the constrictor. Therefore, it seems this phenomenon does not occur very often. The angle with the anode surface was a result of the interaction of this attachment and the cold gas flow. In the case of an upstream attachment the column seemed to be blown through the constrictor by the high velocity of the gas stream. The upstream arc attachment was probably initiated by a turbulent flow, whereby the arc column might have hit the anode upstream in the constrictor.

Electron Temperature from Electron Continuum Intensity Measurement

The spectral continuum emission in a plasma is the sum of two different sources: 1) free-free continuum (Bremsstrahlung) of electrons and 2) free-bound radiation (recombination continuum) of electrons recombining with ions. Continuum radiation from the H_2 molecules is not considered due to their negligible contribution.[11] Quantitatively the emission for an optical thin layer is described by Ref. 12 (p. 34 equation 107 and p. 40 equation 126):

$$\varepsilon_\gamma = \frac{128\pi^4 m_0 e_0^{10}}{c_0^3 h^2 (6\pi m_0 k)^{3/2}} \frac{n_e n_{z,1} z^4}{T_e^{3/2}} \exp\left(\frac{\chi_{z-1} - h\gamma}{kT_e}\right) \times \sum_n G_n(\gamma) n^{-3} \exp\left(-\frac{E_n}{kT_e}\right) + \frac{16\pi e_0^6}{3c_0^3 (6\pi m_0^3 k)^{1/2}} \times z^2 \frac{n_e n_z}{T_e^{1/2}} \exp\left(-\frac{h\gamma}{kT_e}\right) \quad (1)$$

Here the first term represents the free-bound continuum, while the second describes the free-free "Bremsstrahlung." The Gaunt factor $G_n(n)$ is set to unity.[13]

With Eq. (1) the emission can be calculated for a specific temperature and particle density under the partial local thermodynamic equilibrium (PLTE) assumption. Consequently, this expression was combined with a particle density calculation to compare the predicted emissivities with the measured ones. Therefore, the number densities of the plasma species, i.e., electrons, hydrogen atoms, ions, and hydrogen molecules were calculated as functions of temperature and pressure with the method developed by Frie for hydrogen.[10] From Dalton's

law, the condition of local electrical neutrality and the mass action laws (extended Saha equation), a system of equations was derived that allowed the particle density calculation for a given temperature and pressure. This method, which is valid only for local thermodynamic equilibrium (LTE), has been applied here despite the fact that its application to conditions at the edge below about 9000 K turns out to be highly questionable. A more rigorous approach of a nonequilibrium consideration would require much more effort and would lead again to uncertainties.

For this purpose, the calculated spectral emissivities were folded with the transmission function of the 600-nm intensity filter used in the experiments. These spectral emissivities were integrated to reveal the filtered emission coefficient. The corresponding measured value followed from the measurements with the CCD camera after the Abel inversion of the measured intensities.

For the experiments the camera gain was set constant at the same level as during the calibration to avoid linearity problems. Several frames were recorded for later evaluation. In one frame the arc area was selected in order to take single radial profiles. With the calibration results the measured intensities were assigned to the absolute filtered specific intensities. Subsequently, the profiles were Abel inverted[14] to reveal the emission coefficients as a radial function. These were compared with the calculated emissivities described above, resulting in a radial temperature distribution in the arc.

The indicated errors were obtained from calculating or estimating the magnitude of the following contributions: 1) statistical errors of the intensity measurements, estimated to be 5%, resulting from the error of the standard light source and the uncertainties of the calibration procedure; and 2) approximately 15% uncertainties in the calculation procedure of the continuum intensity. This results in an overall error of about ±700 K.

With this method one gets a two-dimensional electron temperature profile in the center part of the constrictor. Figure 5 shows radial temperature profiles at different distances from the cathode tip for a current of 50 A. The temperature in the center column is higher near the cathode and becomes lower

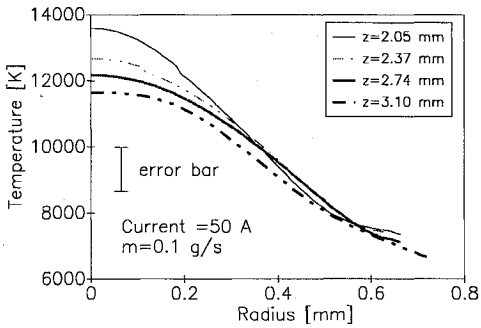

Fig. 5 Radial electron temperature profiles I = 50 A, m = 0.1 g/s.

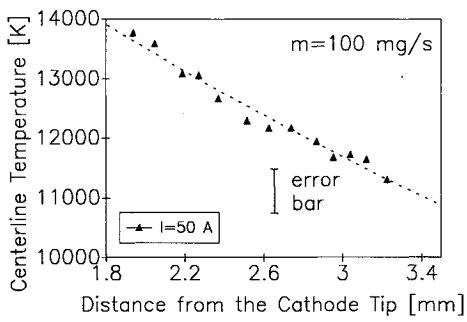

Fig. 6 Electron temperature of the centerline I = 50 A, m = 0.1 g/s.

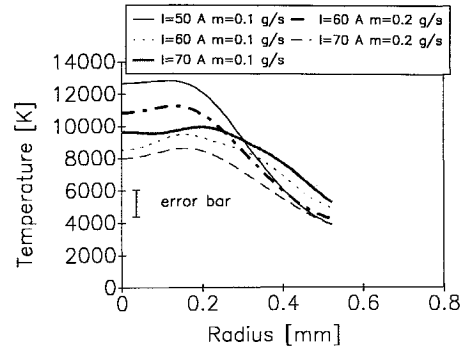

Fig. 7 Electron temperature profiles of different operation points at the same geometrical position.

downstream. This behavior is illustrated in Fig. 6. There the centerline temperature is depicted at different axial positions.

In Fig. 7 the electron temperature profiles for the different arc currents at the same location are shown. It can be seen that the centerline temperature for the same mass flow rate decreases with increasing current; however, the profiles become wider with higher currents. With a higher mass flow rate the arc temperature is lower. The experiments show that the centerline temperature for all investigated cases is less than 14,000 K and does not significantly increase with current. One may explain this behavior in the following way: between 11,000 and 13,000 K the degree of ionization increases from 10 to 30%, and the heat conduction increases by a factor of 2.5 caused by transport of ionization energy. As a consequence of a current increase one should therefore expect a flattening and broadening of the temperature profile, but no increase of the maximum temperature.

Excitation Temperature Determination from Line to Line Intensity Ratios

In addition to the continuum analysis, an attempt was made to determine the excitation temperature profiles of the hydrogen atoms in the discharge channel from the intensity ratio of the spectral lines. As mentioned above, the arc emission was measured not only in the broadband mode and through the continuum filter, but also through three narrow band interference filters centered around the three strongest hydrogen lines H_α (656 nm), H_β (486 nm), and H_γ (436 nm). The filter width of 10 nm is sufficient to include the line broadening due to the Doppler and Stark effects.[12]

A word of caution appears necessary regarding the data reduction procedure described below. The temperature equation [Eq. (2)] implies the existence of two isolated spectral lines. This is not precisely true for the arc emission since some broadband background radiation also exists, which contributes to the emission intensities passing through the interference filters. It is assumed that this background radiation is sufficiently small (as calculations show less than 3%) and can be neglected. A second problem arises from the assumption of optical transparency of the plasma, which has to be satisfied for the applicability of the Abel inversion. It could be possible that the discharge column is optically "thick" (absorptive) for the center of the line. The optical depth is calculated to be a factor of 10 larger for the H_α line than the geometrical dimension of the arc. Therefore, the plasma can be taken as transparent and the Able inversion can be applied.

Under the assumption of local thermal equilibrium the atomic excitation temperature of the hydrogen atoms can be derived from the intensity measurements for two spectral lines according to Griem[13] (equation 13.1):

$$T_{ex} = \frac{1}{k} \frac{E_2 - E_1}{\ln\left[\left(\frac{I_1}{I_2}\right)\left(\frac{\lambda_1}{\lambda_2}\right)^3 \frac{g_2 f_2}{g_1 f_1}\right]} \qquad (2)$$

The intensity profiles were extracted from the line scan profiles as described above, using the shift-and-average technique on a sample of 200 scans for each wavelength. The measured intensities were converted to absolute filtered intensities with the calibration results. Subsequently, the profiles were Able inverted to reveal the absolute intensities for each line. According to Eq. (2) the radial excitation temperature distribution was calculated from the radial intensity distributions.

An error calculation, taking into account the contribution from the different input parameters, revealed an uncertainty of about ± 900 K for the line ratio method.

The method worked well for the temperature determination from the H_α/H_β ratio. However, the measured H_γ line intensity was too low to allow a reliable temperature determination. Temperature gained from the H_β/H_γ and H_α/H_γ intensity ratio varied from 4000 K up to 6000 K. The difference between these temperature sources indicates that the population of the upper H_γ level (fifth energy level in the H-atom) is not in equilibrium with the third and fourth energy level. This discrepancy may be explained by examining the time scale of different processes in the constrictor. The distance of the observation region to the cathode tip is approximately 1.6 mm. It seems reasonable that the hydrogen velocity in the arc column of the constrictor region may be assumed to be in the range of sonic velocity (about 8000 m/s). Thus, the atoms need approximately 2×10^{-7} s to move from the cathode tip to the observed region. The process of depopulation of the fifth energy level through emission of an H_γ-light quant, however, has a time scale of the same magnitude and is a factor of five slower than the H_β-emission process.[15] If one considers additionally the fact that the population of the fifth level through collision or radiative decay from higher energy levels is slower by a factor of five than the approximated mechanism for the H_β or H_α line, it seems to be consistent to neglect the H_γ measurements due to an under population of the fifth energy level.

The radial excitation temperature profile for three of the investigated operation points gained from the H_α/H_β ratio are shown in Fig. 8. They show the same behavior as the electron temperature determined from the continuum radiation. The temperature decrease in the centerline is within the measurement accuracy and may be caused by the analysis procedure. In Fig. 9 the results of the excitation temperature determination are compared with the electron temperature. Within the limits of the measurement accuracy of both methods the centerline temperatures are the same. However, at the edge, the electron and the excitation temperature deviate. The electron temperatures are higher than the excitation temperatures. This is a strong indication that at the edge, high-energy electrons are still available which recombine with residual ions, while excited atoms are less populated in the outer region. Thus, in the edge region of the arc corona conditions prevail over Saha conditions.

The results are comparable to those of Wiese et al.,[15] who investigated a hydrogen arc column of 40 A at a pressure of 1 bar. They found a centerline temperature of 12,600 K from hydrogen H_α and H_β line measurements.

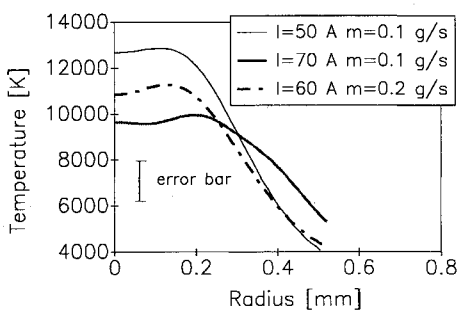

Fig. 8 Radial excitation temperature profiles from line ratio.

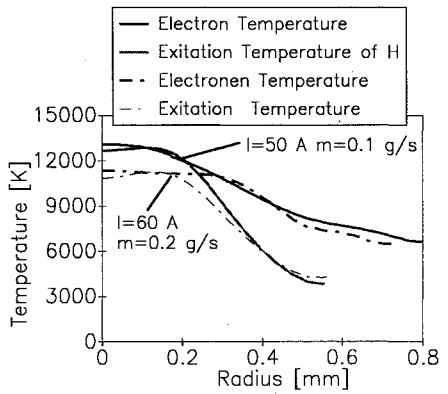

Fig. 9 Comparison of electron and excitation temperatures.

Theoretical Modeling

The performance of a thermal arcjet thruster is strongly determined by the processes in the constrictor. To provide a basic understanding of the overall arcjet behavior and to provide the engineers with design criteria for a constrictor-type arcjet thruster, a numerical model of the arc in the constrictor was developed and the calculation results were compared with experiments.

The constrictor conditions are characterized by an electric arc within an axial flowfield. The main energy input into the propellant takes place in the constrictor and the supersonic flow can be approximated by frozen flow conditions due to the low density and the high gas velocity in that part of the nozzle. The anode attachment is assumed to be behind the downstream end of the constrictor and to have no significant influence on the overall behavior of the thruster, because the pressure decreases rapidly, and therefore, the coupling between electrons and the heavy particles becomes weaker.

Constrictor Conditions

A three-channel model is derived from the dual channel model.[7] With this three-channel approach the flow in the constrictor is divided into three parts (see Fig. 10), which are separated by constant temperature lines. The first channel is the hot current conducting arc column, which is surrounded by a noncurrent conducting channel where dissociation reactions are dominant. The boundary between these layers was set to 7000 K. This channel is again surrounded by a cold gas layer with a uniform temperature. For the calculation of a water-cooled thruster this temperature was set to 250 K, whereas for radiation cooled thrusters this temperature has to be set to much higher levels.

By solving the energy equation for each channel separately, one gets the two-dimensional temperature distribution inside the constrictor. The model is developed for hydrogen as propellant, but it can be extended for other propellants by ex-

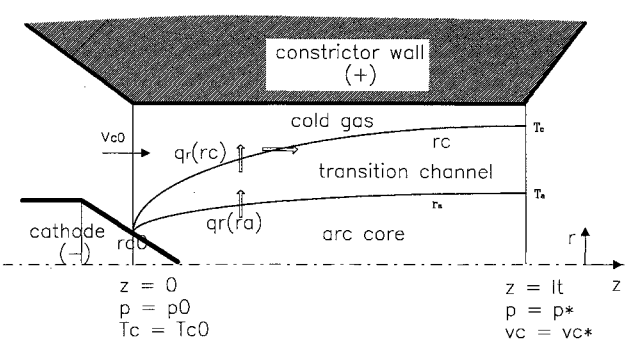

Fig. 10 Schematic of the constrictor condition.

changing the thermal properties. The number densities of the plasma species were calculated as functions of temperature and pressure with the method developed by Frie[16] as described below. With these calculated particle densities the heat conduction coefficients are derived according to Ref. 17 and the electrical conductivity as described in Ref. 8.

Hot Arc Column

The governing energy equations are those of the heavy particles and the electrons. Since the electron gas is directly affected by ohmic heating and since it is electrostatically coupled to the positively charged ions, the convective energy of the electrons can be neglected against that of the much heavier ions. Assuming thermal equilibrium ($T = T_e$), the simplified electron energy equation reduces therefore to the Elenbaas-Heller equation:

$$\frac{1}{r}\frac{\mathrm{d}}{\mathrm{d}r}\left(r\lambda_e\frac{\mathrm{d}T}{\mathrm{d}r}\right) + \frac{j^2}{\sigma} - RL = 0 \tag{3}$$

Using the analytical solution developed for the dual channel model under the assumption of a parabolic current density distribution, one gets the temperature profile in the arc core

$$\int_T^{\hat{T}} \lambda\,\mathrm{d}T = \frac{1}{\hat{\sigma}}\left(\frac{n+2}{n}\right)^2\left(\frac{I}{\pi r_a^2}\right)^2\frac{r^2}{4} \times\left[1 - \frac{4}{(n+2)^2}\left(\frac{r}{r_a}\right)^n - \zeta(r)\right] \tag{4}$$

For a given temperature at the boundary (T_a) the centerline temperature can be calculated from

$$\hat{\sigma}\int_T^{\hat{T}} \lambda\,\mathrm{d}T = \left(\frac{n+2}{n}\right)^2\left(\frac{I}{2\pi r_a}\right)^2\left[1 - \frac{4}{(n+2)^2} - \zeta(r_a)\right] \tag{5}$$

The radial heat flux by heat conduction to the transition layer is given by

$$q_r(r_a) = \frac{1}{\hat{\sigma}}\frac{I^2}{2\pi^2 r_a^3}\left[\frac{n+2}{n} - \left(\frac{n+2}{n}\right)^2\bar{\zeta}\right] \tag{6}$$

The velocity in the arc core is assumed to be the speed of sound under isothermal conditions.

Transition Region

The energy equation for the transition region is given by Eq. (7) under the assumption that the radial velocity is low compared to axial one and that the axial temperature gradient is low compared to the radial one. Convection and radiation losses are neglected:

$$\frac{1}{r}\frac{\mathrm{d}}{\mathrm{d}r}\left(r\lambda\frac{\mathrm{d}T}{\mathrm{d}r}\right) = 0 \tag{7}$$

The radial heat flux is completely conducted through the transition region into the cold gas layer. Introducing a potential function for the heat flux

$$\Theta = \int_{T_\infty}^{T} \lambda\,\mathrm{d}T \tag{8}$$

the radial temperature distribution in this channel can be derived from the energy equation:

$$\Theta_a - \Theta = r_a q_r(r_a)\,\ln(r/r_a) \tag{9}$$

The boundary r_a of the current conducting channel can be calculated iteratively from the expression

$$r_a = r_c \exp\left[-\frac{\Theta_a - \Theta_c}{r_a q_r(r_a)}\right] \tag{10}$$

The velocity in this region is assumed to change with temperature between the speed of sound at the inner boundary and the cold gas velocity at the outer boundary.

Cold Gas Layer

It is assumed that the main part of the cold gas layer is completely unaffected and that the radial heat flux is "deposited" on the axial flowing cold gas in a small layer around the transition region and convected downstream. A solution of the energy equation for this region is described in more detail.[8] This results in the following terms, describing the contour of the cold gas depending on the radial heat flux:

$$z - z_0 = \frac{1}{8}\kappa^{3/2}\left(\frac{2}{\kappa-1} + Ma^2\right) \times Ma\sqrt{\frac{\mathcal{R}}{M}}\frac{p}{\lambda\sqrt{T_c}}\left(\frac{r-r_c}{r_c}\right)^2\frac{r_c^2}{X^2} \tag{11}$$

with

$$X^2 = 2.2688\,(\sqrt{1 - 0.570125\,\ln|Y|} - 0.981574)^2 \tag{12}$$

$$Y = \frac{\lambda\Delta T}{r_c q_r(r_c)}\left(\frac{r_c}{r-r_c}\right) \tag{13}$$

The velocity in the cold gas layer is described by a quasi-one-dimensional flow theory under adiabatic conditions:

$$v_{z,c2}^2 - v_{z,c1}^2 + \frac{2\kappa}{\kappa-1}\frac{p_1}{\rho_1}\left\{\left(\frac{p_2}{p_1}\right)^{[(\kappa-1)/\kappa]} - 1\right\} = 0 \tag{14}$$

The three channels are linked together assuming constant pressure in each cross section and by the conservation of mass:

$$\dot{m} = (\dot{m}_a + \dot{m}_{tr}) + \dot{m}_c = 2\pi\frac{p}{\sqrt{\mathcal{R}}}\int_0^{r_c}\sqrt{\frac{M}{T}}\,Ma\,\mathrm{d}r + v_{z,c}\frac{p}{(\mathcal{R}/M)T_\infty}\pi(r_t^2 - r_c^2) \tag{15}$$

The cold gas velocity and the pressure in each cross section can be calculated from Eqs. (14) and (15).

The radial step size parameter $(r - r_c)/r_c$ in the cold gas contour Eq. (11) is chosen such that the critical point in the cold gas is achieved at the constrictor end.

With this model the thermal properties at the constrictor end for a given cold gas enthalpy in the arc chamber can be determined. The expansion in the diverging part of the nozzle is calculated for a quasi-one-dimensional flow under frozen flow conditions. The thrust as an integral value is calculated according to

$$T = 2\pi\int_0^{r_e}\rho_e v_e^2 r\,\mathrm{d}r + \pi\rho_{e,c}v_{e,c}^2(r_e^2 - r_c^2) + \pi p_e r_e^2 \tag{16}$$

Results, Comparison with Experiments

The theoretical and the experimental data of the described water-cooled TT1 thruster are compared. For this thruster

the overall data are well known over a wide range of parameters, and the data inside the arc chamber and the constrictor are also well known.[9]

The geometry of the thrusters

Constrictor radius:	$r_t = 1.25$ mm
Constrictor length/constrictor radius:	$l/r_t = 4$
Exit area/throat area	$A_e/A_t = 100$

Table 2 shows the calculated thrust compared with measurements of the TT1 thruster for some edge points. The calculated thrust agrees well with the measured one despite the crude mathematical model.

The results of the operation point 50 A and 0.1 g/s will be presented in more detail. In Fig. 11 the development of the channel boundary is shown. It can be seen that the arc diameter increases much steeper near the cathode than further downstream. The pressure decrease inside the constrictor as well as the increase of the heated mass flow are nearly constant (Fig. 12). But at the end of the constrictor more than 60% of the propellant is still not directly affected by the heating.

In Fig. 13 the calculated temperature profile is compared with the measured profile. The measured one is lower at the center, but shows the same behavior and the diameter of the resulting arc channel is nearly the same. The higher centerline temperature indicates that the heat flux into the transition region is in reality larger than the modeled one. This may be due to the influence of convective cooling, which is not considered for the two inner channels. The calculated temperature profiles have a significant plateau caused by dissociation reactions in the transition region.

Table 2 Comparison of the measured and the calculated operation points

Current, A	50	151	67	138
Mass flow, g/s	0.1	0.1	0.2	0.2
Pressure, mbar	943	1227	1477	1686
Thrust (experimental), N	0.63	0.92	0.94	1.19
Thrust (calculated), N	0.686	0.876	1.068	1.198
Discrepancy, N	0.056	0.044	0.128	0.008

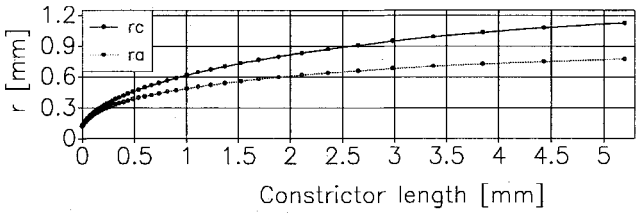

Fig. 11 Boundary of the arc channels.

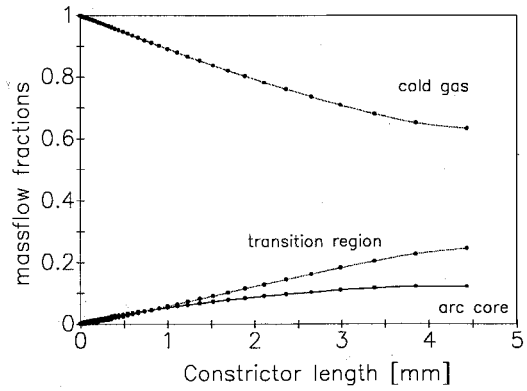

Fig. 12 Calculated mass flow fractions in the constrictor.

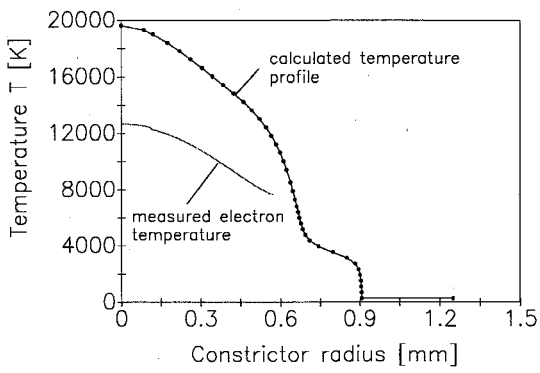

Fig. 13 Comparison of the calculated and the measured temperature profiles.

Conclusions

A direct observation of the arc in the constrictor as well as the analysis of the discharge column provide spatially resolved data in this crucial part of the arcjet thruster. The electron temperature distribution and the excitation temperature of the hydrogen in the constrictor were determined and it was found that at the edge of the arc column there is thermal nonequilibrium.

Important insights have been provided into the physics of the arc in the constrictor and the energy transport in this region by the theoretical model. The consistency of calculated and measured thrust is fairly good. The three-channel model has therefore proved to be a reliable instrument for the optimization of thermal arcjet thrusters.

Acknowledgments

The authors would like to thank D. Keefer and D. Zube for their support and the fruitful discussions in spectroscopy, Th. Rösgen for advice on the data reduction, and H. O. Schrade and B. Gaus for their support in the theoretical modeling.

References

[1]Thahara, H., Sakakibara, T., Onoe, D., and Yoshikawa, T., "Discharge Characteristics and Inner Plasma Features of a High-Power DC Arcjet Thruster," AIAA Paper 90-2534, 1990.

[2]Thahara, H., Sakakibara, T., Onoe, K., and Yoshikawa, T., "Experimental and Numerical Studies of a 10 kW Water-Cooled Arcjet Thruster," 22nd International Electric Propulsion Conf., IEPC 91-015, Viareggio, Italy, Oct. 1991.

[3]Krülle, G., "Motion of the Plasma Column in the Interior and the Exit of an Arc Jet," Deutsche Versuchsanstalt für Luftfahrt, Inst. für Plasmadynamik Abschlußbericht RFF 15/2, 1966.

[4]John, R. R., Bennett, S., and Connors, J. F., "Thirty Kilowatt Plasma Rocket Engine Development, Third Year Development," AVCO Corp., Summary Rept., RAD TR-64-6-NASA CR-54044, July 1964.

[5]Glocker, B., and Auweter-Kurtz, M., "Radiation Cooled Medium Power Arcjet Experiments and Thermal Analysis," AIAA Paper 92-3834, July 1992.

[6]Rhodes, R. P., and Keefer, D., "Modelling of a Hydrogen Arcjet Thruster," 22nd International Electric Propulsion Conf., IEPC 91-111, Viareggio, Italy, Oct. 1991.

[7]Butler, G., and King, D., "Single and Two Fluid Simulations of Arcjet Performance," AIAA Paper 92-3104, July 1992.

[8]Glocker, B., Schrade, H. O., and Sleziona, P. C., "Numerical Prediction of Arcjet Performance," AIAA Paper 90-2612, July 1990.

[9]Glocker, B., Rösgen, Th., and Laxander, A., "Medium Power Arcjet Analysis and Experiments," 22nd International Electric Propulsion Conf., IEPC 91-016, Viareggio, Italy, Oct. 1991.

[10]Glocker, B., Auweter-Kurtz, M., Gölz, T. M., Kurtz, H. L., and Schrade, H. O., "Medium Power Arcjet Development," AIAA Paper 90-2531, July 1990.

[11]Wiese, W. L., Paquette, D. R., and Solarski, J. E., "Profiles of Stark-Broadened Balmer Lines in a Hydrogen Plasma," *Physical Review*, Vol. 129, No. 3, 1963, p. 1225.

[12]Holtgreven, L., *Plasma Diagnostics*, North Holland, Amsterdam, 1968, pp. 28–41.
[13]Griem, H., *Plasmas Spectroscopy*, McGraw-Hill, New York, 1964, pp. 269–295.
[14]Montgomery Smith, L., and Keefer, D., "Abel Inversion Using Transform Techniques," *Journal of Quantitative Spectroscopy and Radiative Transfer*, Vol. 39, No. 5, 1988, pp. 367–373.
[15]*Atomic Transition Properties*, U.S. Dept. of Commerce, National Bureau of Standards, Washington, DC, 1966.
[16]Artmann, J., and Bohn, W. L., "Berechnung der Plasmakomponenten in Wasserstoff und Helium," Forschungsbericht 65-10, Deutsche Versuchsanstalt für Luft und Raumfahrt, März 1965.
[17]Yos, J. M., "Transport Properties of Nitrogen, Hydrogen, Oxygen and Air to 30000 K," Research and Advanced Developement Division, AVCO Corp., Contract AF33(616)-7578, Wilmington, MA, 1963.